Evaluation of volume deformation from surface DIC measurement.

M. Rossi[a], L. Cortese[b], K. Genovese[c], A. Lattanzi[a], F. Nalli[d], F. Pierron[e]

[a] *Università Politecnica delle Marche, Ancona, Italy. E-mail: m.rossi@univpm.it*
[b] *Department of Mechanical and Aerospace Engineering, Sapienza University of Rome, Roma, Italy.*
[c] *School of Engineering, University of Basilicata, Potenza, Italy*
[d] *Faculty of Science and Technology, Free University of Bozen - Bolzano, Bolzano, Italy*
[e] *Engineering and the Environment, University of Southampton, Southampton, UK*

Abstract

Stereo-DIC allows to track with a high accuracy the shape change and the surface displacement field of objects during deformation processes. When multiple camera arrangements are used, the shape and deformation measurement can be performed over the whole surface of the object. We submit that, in the case of intact specimens, with no internal defects and/or discontinuities, such boundary information can be used to estimate the internal displacement field by using proper interpolation functions. This calculation could serve, for instance, to evaluate the strain localization that occurs in metal specimens subjected to plastic deformation, hence allowing to get a better insight in the necking initiation and fracture propagation processes. In this paper, an interpolation method based on Bézier curves is developed and tested using simulated and real experiments on specimens with flat and cylindrical geometries. In particular, the deformation behaviour in the necking zone was investigated in the case of highly ductile and anisotropic materials. Numerical models were used to validate the method while the application to two real experiments demonstrated its feasibility in practi-

cal cases. The applicability of the method to more complex loading cases (e.g., bending, torsion, mixed-loads) or different initial shapes (e.g., curved beams, notches) will be investigated in future studies.

Keywords:
stereo-DIC, large deformation, 3D volume reconstruction, necking, Bézier curves

---

1. Introduction

In the recent years, the use of full-field optical techniques to measure the shape, motion and surface deformation of solids has considerably increased. Among the several reasons for its popularity, there are the decreasing cost of the equipment, the increasing performances of digital optical sensors and the wide availability of dedicated commercial and academic software packages for image processing. In engineering, full-field measurements are frequently used for material testing and characterization [1].

Among the full-field optical techniques used in solid mechanics, Digital image Correlation (DIC)[2, 3] is probably the most widespread and fastest-growing method. The DIC technique tracks the displacement of a random speckle pattern that, if not naturally present, can be applied onto the specimen surface using different techniques [2]. If the target surface is flat and the displacement is in-plane, a single camera (2D-DIC) is sufficient for the measurement, otherwise a two-camera arrangement (stereo-DIC) allows to retrieve the shape and track the displacement of the object surface in the three-dimensional space on the basis of the stereo-photogrammetric principles [4].

Such a surface measurement suffers form an important limitation in

material characterization since no information is provided in the bulk of the material. Usually, plane-stress or plane-strain conditions are assumed. However, these assumptions are not always appropriate when, for instance, necking occurs in the plastic deformation regime [5, 6]. Information on the three-dimensional distribution of strain and stress field inside a specimen is also important to calibrate ductile damage models [7, 8].

Commonly, the stress-strain distribution inside solids is computed by Finite Element Method (FEM) analyses. In particular, Finite Element Model Updating (FEMU) approaches can be adopted to iteratively identify the mechanical properties of materials [9, 10]. The main limitations of FEMU, especially for 3D models, are the high computational cost and the mesh sensitivity [11]. If volume deformation was directly evaluated from experiments, more computationally efficient identification methods could be used, *e.g.* the Virtual Fields Method (VFM) [12–15].

Nowadays, the volume deformation of solids can be obtained directly from experiments by Digital Volume Correlation (DVC) [16]. Although this technique is very promising, it presents a series of limitations: it requires expensive and complex equipments (*e.g.* x-ray tomography [17, 18]), the investigated material needs to have a random internal pattern (*e.g.* foams, bones tissue, composites etc.) [19–21] and the correlation algorithm is computationally expensive. Magnetic resonance imaging or magnetic resonance elastography can serve to evaluate the volume displacement too, however their use is usually limited to biological tissues [22]. For most materials of engineering interest such as metals, polymers, rubber, etc., the aforementioned techniques cannot be effectively employed.

In this work, a method is proposed to reconstruct the volume displacement field from surface data. A first attempt in this direction was made

by some of the authors in [23], however, no validation of the method was provided at that time. In this paper, the reconstruction technique is studied in detail, numerical models were used to evaluate the accuracy and the application to two experimental cases are presented and discussed.

In order to apply the proposed volume reconstruction method, it is required to know the displacement field over the whole external surface of the investigated solid. To this purpose, different approaches can be used: (i) the object is surrounded by a multi-camera arrangement [24–26], (ii) a single camera is rotated about the object [27–29], (iii) the camera is fixed and the object is rotated by using a rotation stage [30–32]. The latter method cannot be adapted to a standard tensile machine, therefore only the first two approaches will be used in the experiments. Multiple optical methods could also be used, as for instance in [33, 34] where a combined use of DIC and fringe projection was employed to improve the accuracy of the object surface reconstruction.

The paper is organized as follows: in Section 2, a detailed description of the proposed reconstruction method is reported, a numerical validation is performed in Section 3 and finally, in Section 4, the experimental results are presented and discussed.

2. Methods

The proposed algorithm was developed with the aim to reconstruct the volume displacement field inside a solid starting from surface measurements. In the version described here, it can be applied to basic geometries that undergo large (*e.g.* plastic or hyperelastic) deformation. The method generates internal nodal points with positions that are changed according to surface

information, therefore it will be referred to as Internal Mesh Generation (IMG) method. Two test cases were considered: an initially flat specimen where the displacement field is measured on the two opposite faces and an initially cylindrical specimen, where the full-field displacement is known for the whole 360-deg surface. The reconstruction algorithm varies in the two cases, as described below.

2.1. Flat specimens

In the initial undeformed configuration, flat specimens have a constant thickness and two opposite parallel faces. In order to apply the IMG method, the displacement field has to be known on both faces, named here Face A and Face B. Figure 1 shows a schematic of the measurement point grids obtained in the two faces in the initial and deformed configuration. The coordinate system is chosen so that the z-axis is perpendicular to the thickness at the beginning of the test. Let us consider a point $\mathbf{N}_A$ in Face A and the corresponding opposite point $\mathbf{N}_B$ in Face B. According to the selected coordinate system, at the beginning, $\mathbf{N}_A$ and $\mathbf{N}_B$ have the same $\{x, y\}$ coordinates and different z. As deformation occurs, the spatial coordinates $\{x, y, z\}$ of $\mathbf{N}_A$ and $\mathbf{N}_B$ can be evaluated at each load step from the full-field displacement measurement.

In order to generate the internal mesh, the method exploits quadratic Bézier curves defined starting from three points, which are $\mathbf{N}_A$, $\mathbf{N}_B$ and a point $\mathbf{P}$ inside the volume. The resulting curve $\mathbf{B}(t)$ is described by the following equation:

$$\mathbf{B}(t) = (1-t)^2\mathbf{N}_A + 2(1-t)t\mathbf{P} + t^2\mathbf{N}_B \;\text{ with }\; 0 \leqslant t \leqslant 1 \qquad (1)$$

where t is a parameter that varies from 0 to 1, so that $\mathbf{B}(0) = \mathbf{N}_A$ and

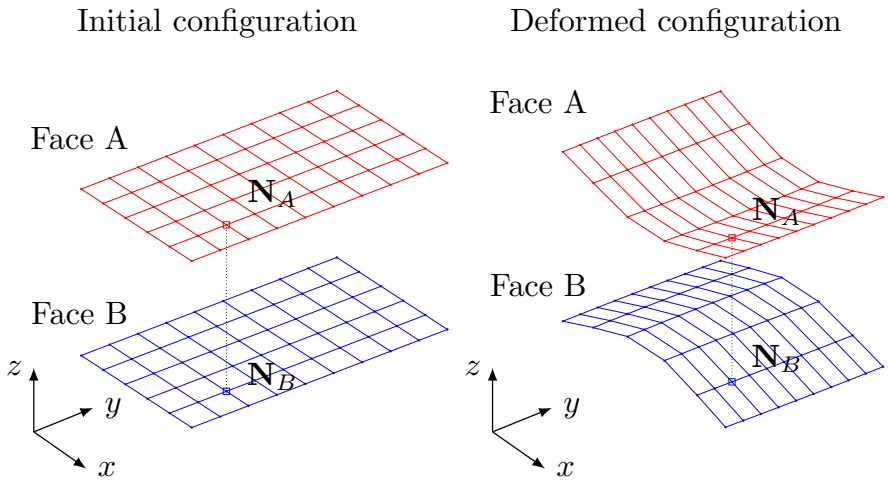

Figure 1: Identification of points $\mathbf{N}_A$ and $\mathbf{N}_B$ in the two faces of the specimen.

$\mathbf{B}(1) = \mathbf{N}_B$. An important property of quadratic Bézier curves is that the curve is tangent to segment $\overline{\mathbf{N}_A\mathbf{P}}$ at the starting point $\mathbf{B}(0)$ and to segment $\overline{\mathbf{N}_B\mathbf{P}}$ at the end point $\mathbf{B}(1)$.

The definition of the Bézier curves and the internal mesh generation process is illustrated in Figure 2, for the initial and deformed configurations. For the sake of clarity, the point of view is chosen perpendicular to the y-direction, however points and vectors are considered in the three-dimensional space. The internal point $\mathbf{P}$ is defined as the intersection between the straight line perpendicular to Face A (or Face B) in $\mathbf{N}_A$ (or $\mathbf{N}_B$) and the mid-plane perpendicular to segment $\overline{\mathbf{N}_A\mathbf{N}_B}$. In the initial configuration, the specimen is flat and $\mathbf{N}_A$ is opposite to $\mathbf{N}_B$, thus the coordinates of point $\mathbf{P}$ are:

$$\mathbf{P} = \frac{\mathbf{N}_A + \mathbf{N}_B}{2} \tag{2}$$

and the resulting Bézier curve is a straight line from $\mathbf{N}_A$ to $\mathbf{N}_B$. In the de-

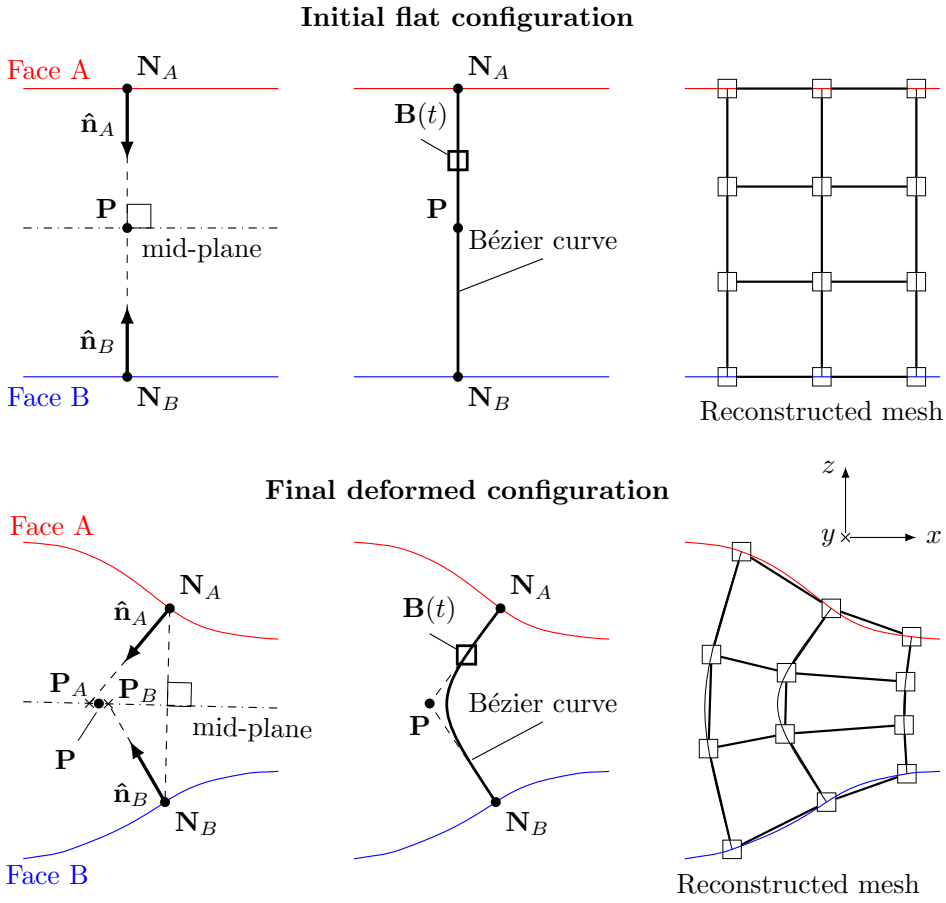

Figure 2: Schematic of the reconstruction method for flat specimens.

formed configuration, instead, the two surfaces are not flat and two different points $\mathbf{P}_A$ and $\mathbf{P}_B$ are obtained depending on whether starting from Face A or Face B, see Figure 2. If $\hat{\mathbf{n}}_A$ and $\hat{\mathbf{n}}_B$ are the normals to Face A and Face B at points $\mathbf{N}_A$ and $\mathbf{N}_B$ respectively, according to geometrical considerations, it follows:

$$\mathbf{P}_A = \mathbf{N}_A - \frac{|\mathbf{N}_A - \mathbf{N}_B|^2}{2\,(\mathbf{N}_A - \mathbf{N}_B)\cdot\hat{\mathbf{n}}_A}\hat{\mathbf{n}}_A \tag{3}$$

$$\mathbf{P}_B = \mathbf{N}_B - \frac{|\mathbf{N}_B - \mathbf{N}_A|^2}{2\,(\mathbf{N}_B - \mathbf{N}_A)\cdot\hat{\mathbf{n}}_B}\hat{\mathbf{n}}_B \tag{4}$$

where $\cdot$ is the scalar product. Point $\mathbf{P}$ is finally computed as[1]:

$$\mathbf{P} = \frac{\mathbf{P}_A + \mathbf{P}_B}{2} \tag{5}$$

It may be be noted that, if the deformation of the two surfaces was symmetrical, as theoretically occurs in necking of isotropic materials, $\mathbf{P}_A$, $\mathbf{P}_B$ and $\mathbf{P}$ would be coincident. However, this is not usually true because of the measurement errors and the possible anisotropic or heterogeneous behaviour of the material.

For each load step, a different Bézier curve is generated for each pair of points in the two faces. As illustrated in the second schematic of Figure 2, parameter t identifies a specific point of curve $\mathbf{B}(t)$. We assume that a given point is identified by the same value of t during deformation, *i.e.* its position can be tracked at different steps of the test using the same t in the

[1]Note that each point can be regarded as a position vector respect to the origin $\mathbf{O}$, *e.g.* $\mathbf{P} = \overrightarrow{\mathbf{OP}}$. For the sake of clarity $\mathbf{O}$ is omitted, however all terms of Eqs. 3, 4 and 5 and following are actually vectors.

corresponding curve. This assumption was found to be reasonable following the reconstruction validation presented later on using numerical models. It is interesting to note that similar approaches can be found in the literature in [35, 36] in the case of necking and strain localization.

Choosing a suitable number of internal points, as illustrated in the last schematic of Figure 2, a 3D mesh can be assembled where the position of each node is known for every step of the test. If $\mathbf{X}_0$ is a point in the initial configuration and $\mathbf{X}_1$ is the corresponding point in the deformed configuration, the displacement vector $\mathbf{u}$ is:

$$\mathbf{u} = \mathbf{X}_1 - \mathbf{X}_0 \tag{6}$$

The displacement and strain fields inside the body can be retrieved using 3D shape function similarly to FEM analysis.

2.2. Cylindrical specimens

The IMG method can be adapted to derive the volume deformation of cylindrical objects using simple assumptions. Figure 3 describes the procedure. In this case, the initial geometry is a cylinder, the measurement points are placed on a regular cylindrical grid along the 360-deg external surface and the initial coordinate system is defined so that the z-axis coincides with the cylinder axis. $\mathbf{N}_A$ and $\mathbf{N}_B$ become two opposite points in one circumference of the cylindrical grid. For each circumference, there will be n pairs of $(\mathbf{N}_A^{(i)}, \mathbf{N}_B^{(i)})$ with $i = [1, \ldots, n]$.

As a first step, the central axis perpendicular to the circumferential plane has to be identified. This is straightforward for the initial configuration, but not for the deformed one, because the section is not necessarily circular anymore. However, many algorithms are available to identify a cylindrical

axis from point clouds [37]. In this work, a 3D fitting algorithm that exploits the minimization of an error function was used, (the details can be found at https://geometrictools.com/Documentation/CylinderFitting.pdf). Afterwards, the coordinates of $(\mathbf{N}_A^{(i)}, \mathbf{N}_B^{(i)})$ are rewritten in terms of cylindrical coordinates $\{r, \theta, z\}$ with respect to the identified axis. For each pair $(\mathbf{N}_A^{(i)}, \mathbf{N}_B^{(i)})$, the reconstruction is performed in the r-z plane, reducing the problem to a 2D one. Point $\mathbf{P}^{(i)}$ is obtained as in the previous section using the normals to the two faces, that are now two profiles in the r-z plane. Finally, a point $\mathbf{P}$ is generated as the average of the $\mathbf{P}^{(i)}$ coordinates.

For each pair $(\mathbf{N}_A^{(i)}, \mathbf{N}_B^{(i)})$, a Bézier curve is created in the $\{r, z\}$ 2D system using $\mathbf{P}$ as central point. A given set of internal points are hence generated using parameter t as explained before. Eqs. 1, 3, 4 and 5 remain the same with the only difference that the points and vectors have 2 components instead of 3. Finally, the generated $\{r, z\}$ coordinates are transformed back to the corresponding Cartesian coordinates $\{x, y, z\}$. For each point, the coordinate $\theta_A^{(i)}$ $(\theta_B^{(i)})$ is assumed to be the same as that of the corresponding $\mathbf{N}_A^{(i)}$ $(\mathbf{N}_B^{(i)})$.

3. Numerical validation

The proposed reconstruction algorithm is based on pure geometrical information (*i.e.* surface displacement and local curvature). In order to evaluate its accuracy when applied to real experiments, the method was first validated using 3D numerical simulation, for which the whole volume deformation history is known. In particular, the test cases simulate the necking evolution in specimens under severe plastic deformation. Two geometries were considered, a flat specimen with an initially rectangular section of

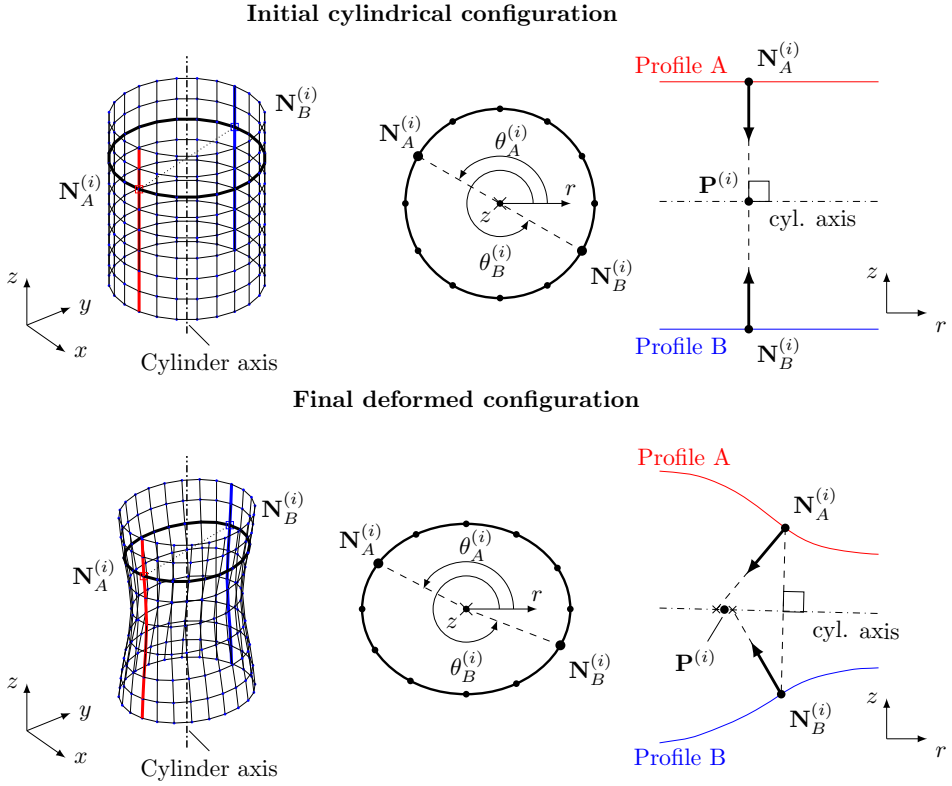

Figure 3: Application of the IGM method for cylindrical geometry.

80×20 mm and a cylindrical specimen with an initial radius of 25 mm. The numerical models were built up using the commercial FE software Abaqus/Standard, adopting 8-nodes brick elements and a constitutive law that describes the behaviour of a metal with high ductility and anisotropy. The Hill48 yielding function [38] was used to describe the yield locus and the Swift power law adopted to describe the stress-strain hardening curve.

Mesh		
	Flat specimen	Cylindrical specimen
Elements	76778	26564
Nodes	85218	29216
Element type	C3D8R	C3D8R
Constitutive law		
Yielding	Hill48	
	$R_0 = 1.8,\ R_{45} = 1.5,\ R_{90} = 2.2$	
Hardening	Swift law	
	$\bar{\sigma} = 700 + 1200\,\bar{\varepsilon}$	

Table 1: Mesh details and material parameters used in the finite element model .

The mesh information and the input constitutive parameters are listed in Table 1, the FE models are illustrated in Figure 4a (flat specimen) and Figure 4b (cylindrical specimen). For both models, the undeformed and deformed configurations are shown in Figure 4 where it is possible to notice that a severe necking occurs at the centres of both specimens. The necking is associated to a complex three-dimensional deformation field as illustrated over the cross sections of Figure 4. The maximum strain is obtained at the inner part of the specimen and thus cannot be directly evaluated by surface

measurements. The value of the equivalent strain is about 1, which falls in the range of the fracture strain observed for ductile metals [39]. The effect of the choice of anisotropic material behaviour for the FE models is particularly evident for the cylindrical specimen for which the deformation is not axisymmetric and the necking section is elliptical.

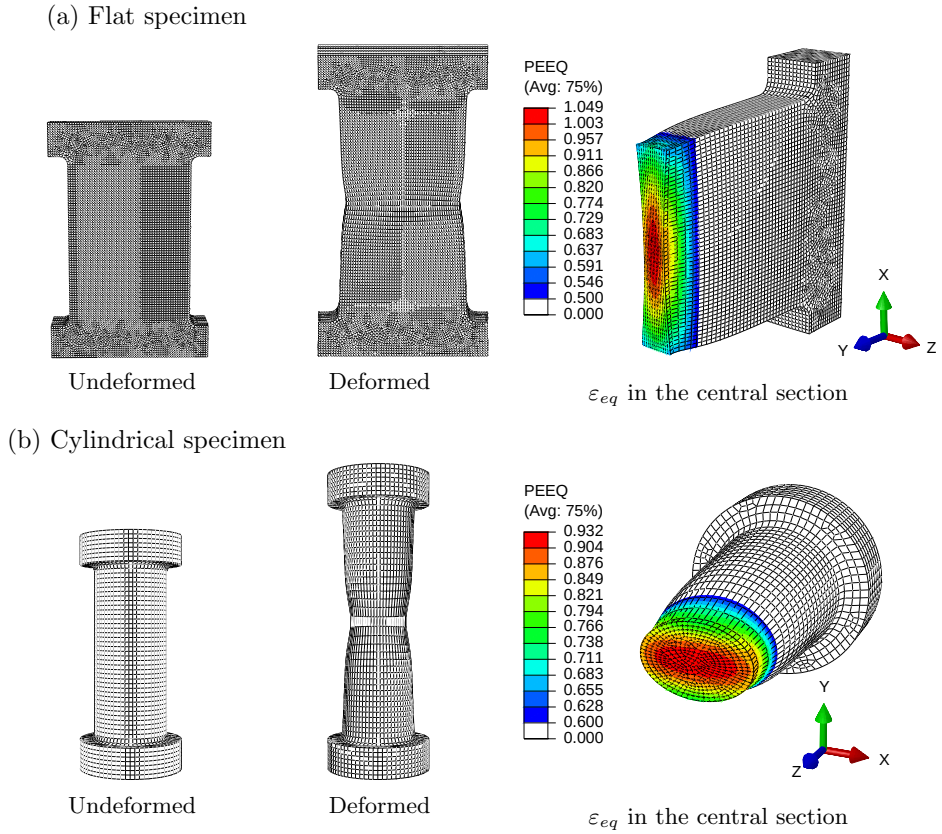

Figure 4: FE models used in the numerical validation, namely a flat (a) and a cylindrical (b) specimen. For each model, the central cross section reveals the strain localization within the necking zone.

The IMG method was used to calculate the internal displacement and strain fields that were compared to their numerical counterparts obtained

from the FEM analyses.

3.1. Flat specimen reconstruction

As is well known, the necking occurs in the central part of the specimen, where the stress/strain state is triaxial and cannot be inferred from surface data. As illustrated in Figure 4, the FE model has a regular hexahedral mesh. The volume of interest (VOI) used to verify the reconstruction algorithm is the central zone where the localized necking occurs. The VOI has 6 nodes along the specimen length (y-direction), 52 nodes along the width (x-direction) and 14 nodes through the thickness (z-direction). The coordinates of the 6×52 nodes belonging to the two external surfaces were used to reconstruct the displacement of the internal nodes. Each Bézier curve was divided in 14 points in order to create a direct correspondence between the FEM nodes and the IMG reconstructed nodes.

Figure 5 shows a picture of the VOI and reconstructed points along the three major section planes. The starting points on the external faces are represented with red square markers, the reference FEM points with blue circles and the IMG reconstructed points with black dots. Plane x-y is the cross section containing the mid-plane and hence all points reported in the plot are the reconstructed/reference ones, no surface data. A reasonably good agreement on the positioning of internal points is observed, with an average error of 0.06 mm (± 0.05 standard deviation).

The capability of the IMG method to reconstruct the internal strain field is shown in Figure 6. The solid lines represent the principal strain evaluated by FEM in the central cross section along two paths, one on the surface and one in the inner part of the specimen, an increase of around 20% is observed in the centre (ε_1 from 0.9 to 1.06). The dashed line represents the

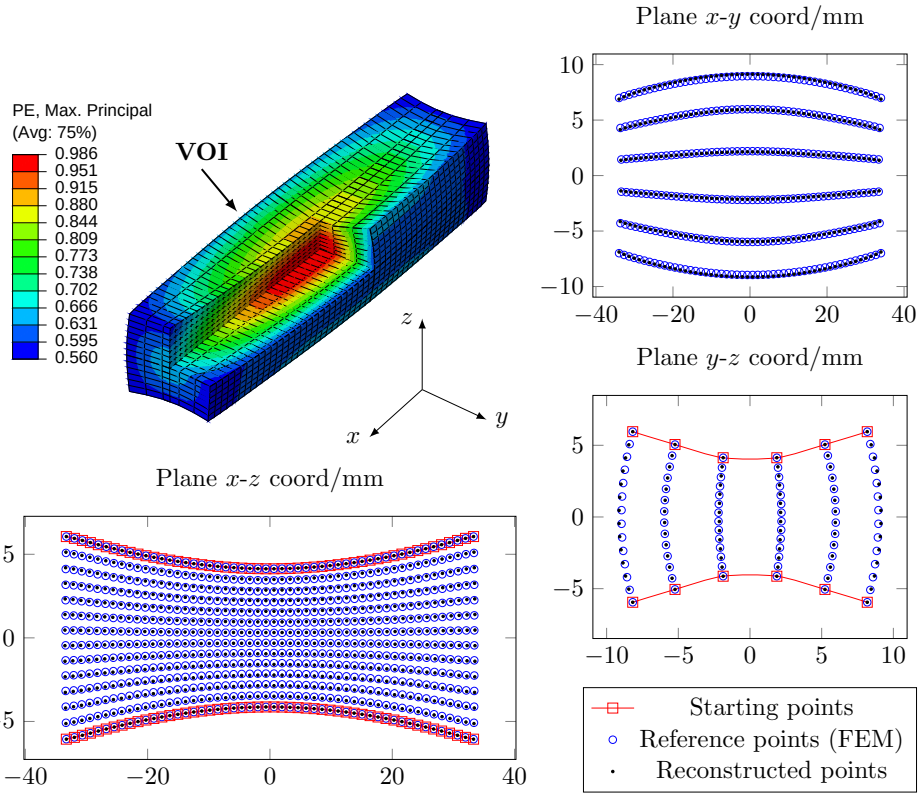

Figure 5: Comparison of reconstructed internal points with the FEM reference data for the flat specimen.

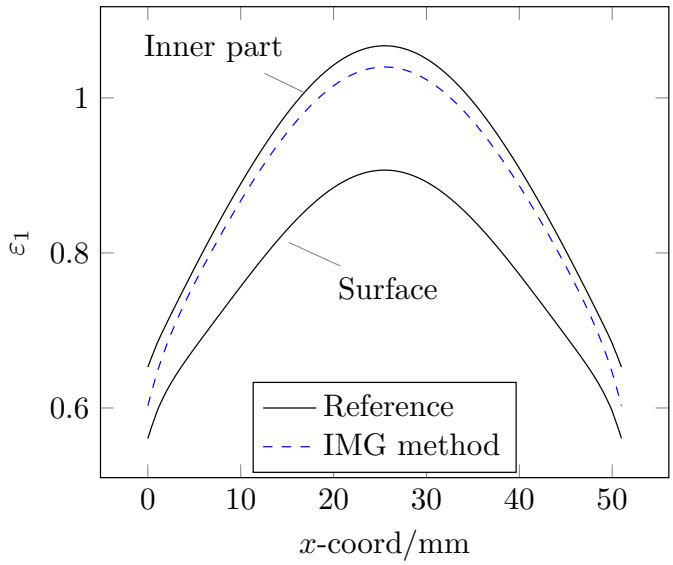

Figure 6: Assessment of the strain field evaluated with the IMG method at the centre of the specimen, where $z = 0$ according to the used coordinate system (see Figure 5).

reconstructed strain in the inner part, the IMG method is able to reproduce the internal localization although it slightly underestimates the maximum value ($\varepsilon_1 = 1.04$ instead of 1.06, 2% error).

It should be underlined that the reconstruction algorithm is purely geometrical and no information on the constitutive model is used. Moreover, the reconstruction of the deformation field inside the necking region of an anisotropic material is not trivial and represents a suitable case study to explore the capabilities of the IMG algorithm.

3.2. Cylindrical specimen reconstruction

A similar validation approach was adopted for the cylindrical specimen. In this case, the whole 360-deg set of surface nodes were used to reconstruct the internal displacement. As in the previous case, only the volume where

the necking occur was reconstructed, the considered VOI has 9 nodes in the axial direction and 24 nodes along the circumference.

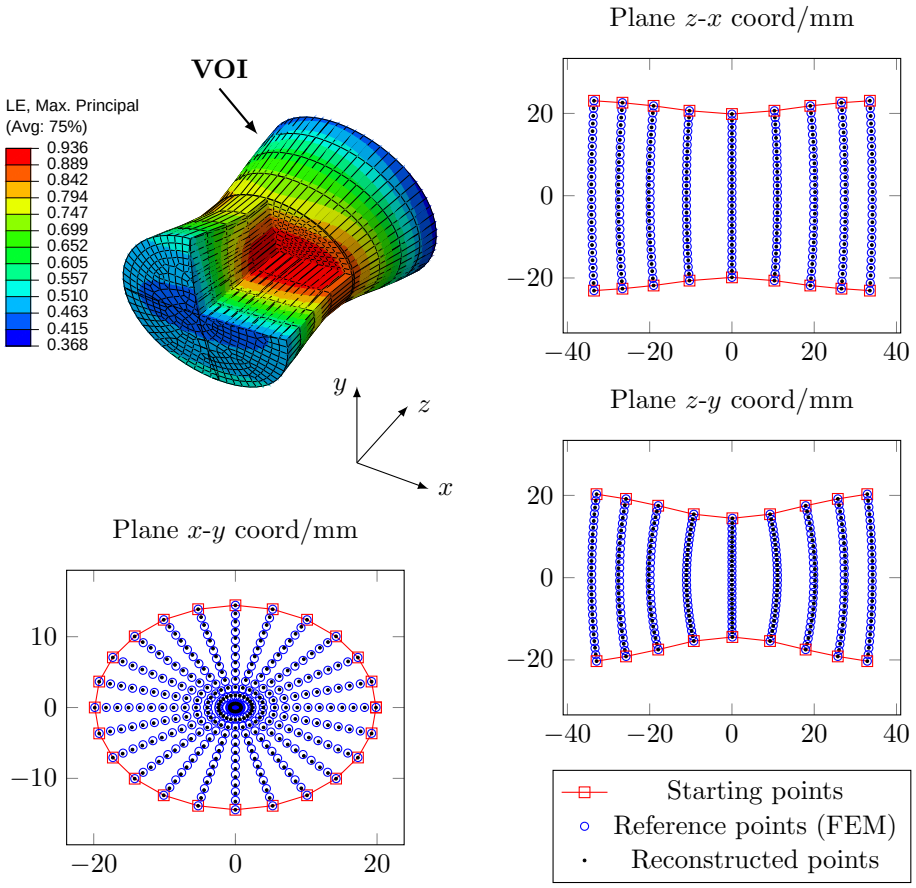

Figure 7: Comparison of reconstructed internal points with the FEM reference data for the cylindrical specimen.

The reconstruction is illustrated in Figure 7 for three section planes. Plane z-x represents a longitudinal section of the specimen across the major axis of the neck, plane z-y a longitudinal section across the minor axis of the neck and plane x-y a cross section in the central part of the neck. The internal nodes were derived following the procedure described in Section 2.2,

using 26 internal points for each Bézier curve. In this case, there is not direct correspondence between internal FE nodes and the reconstructed points. As illustrated in Figure 7, the IMG method for cylindrical specimens produces a distribution of points in the section perpendicular to the axis (see Plane x-y) that is not compatible with a suitable FEM mesh, because the elements in the central zone would have a distorted aspect ratio. The FEM model was therefore built up using an optimal regular mesh, see Figs. 4 and 7.

To allow a quantitative comparison, the displacement field of the FE nodes was remapped according to the position of reconstructed points, using the *scatteredInterpolant* interpolation function implemented in Matlab. If $\mathbf{X}_{\mathrm{FEM}}$ are the coordinates of the FEM nodes in the VOI, $\mathbf{X}_0$ the coordinates of the IMG points in the initial configuration, $\mathbf{u}_{\mathrm{FEM}}$ the displacement field from FEM and $\mathcal{I}$ the interpolation function, it follows:

$$\mathbf{u}_{\mathcal{I}} = \mathcal{I}\left(\mathbf{u}_{\mathrm{FEM}}, \mathbf{X}_{\mathrm{FEM}}, \mathbf{X}_0\right) \tag{7}$$

and

$$\mathbf{X}_{\mathrm{Ref}} = \mathbf{X}_0 + \mathbf{u}_{\mathcal{I}} \tag{8}$$

where $\mathbf{X}_{\mathrm{Ref}}$ are the points used to make the comparison of Figure 7. As for the flat specimen, a fairly good agreement was found, with an average positioning error of 0.09 mm ($\pm$0.08 standard deviation).

The accuracy in terms of strain evaluation is reported in Figure 8, where the first plot shows the two sets of data in the central section of the specimen for two paths along the major and the minor axes of the elliptical section, respectively. Even for this geometry, a reasonably good agreement was found. In particular, it is worth noting that the increase of strain in the central point with respect to the surface is +10% for the major axis and

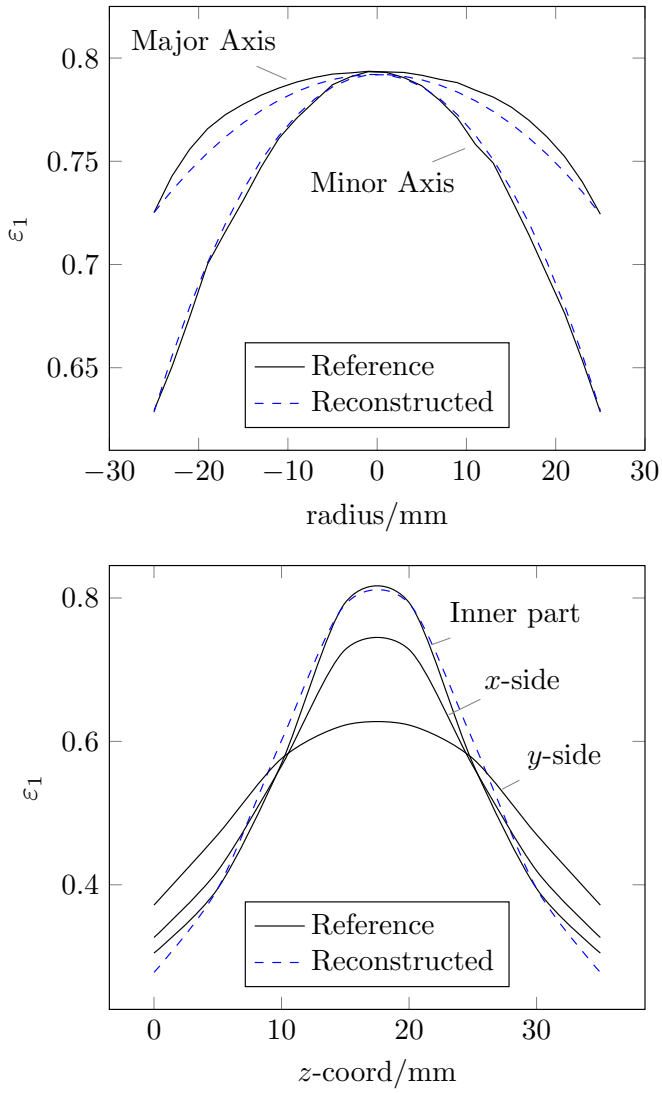

Figure 8: Comparison of the strain field evaluated in the centre of the specimen with the reconstruction method for the cylindrical specimen. Two paths in the central section and a path in the axial direction were evaluated.

+25% for the minor axis.

The second plot of Figure 8 shows the maximum principal strain evaluated along three paths in the axial direction. In particular, the labels "x-side" and "y-side" refer to paths on the external surface of the specimen, while the label "Inner part" refers to the strain evaluated along the central axis of the specimen. Again, a good agreement is obtained using the reconstruction algorithm. The graph clearly shows how, in the necking zone, the state of deformation in the inside of the specimen is largely different from what is observed over the surface and, if the material is anisotropic, a large difference also occurs at different angular positions along the specimen circumference.

Results from the numerical validation demonstrate that the reconstruction algorithm is able to describe with a reasonable accuracy the internal displacement and strain field in the necking zone, although purely based on geometrical surface data. The validation was carried out by considering non trivial case studies including severe necking and anisotropic materials. The reconstructed strain field should be used to identify the material properties through an inverse method like the VFM to check if the level of accuracy is sufficient to use the IMG method for material characterization. Nonetheless, this is beyond the scope of this paper and it will be studied in details in future works.

In the following section, the results of the IMG method as applied to real experiments are reported and discussed.

4. Experimental results

The IMG method starts from the full-field displacement information on the two sides of a flat specimen or on the whole 360-deg surface of a cylindrical specimen. Both cases were considered for this study (see pictures of the experimental set-ups reported in Figure 9).

For the flat specimen (Figure 9a), four identical cameras (JAI Pulnix TM-4000CL, 2048×2048 pixel resolution, 10-bit dynamic range) were used, two for each side of the sample. The four cameras were synchronized and calibrated in order to reconstruct the measured points clouds on the two sides of the specimen in the same coordinate system. The specimen was a flat notched sample obtained from a 3 mm thick sheet metal of 316L stainless steel. It had a minimum width of 18 mm and 11 mm radius notches. The tensile test was conducted using an Instron 880 universal machine. The displacement field over the two faces was obtained using the commercial software Vic3D (http://correlatedsolutions.com/vic-3d/). The reconstruction algorithm was applied to a single deformed configuration. In particular, the chosen load step is just before the final fracture, when the localized necking through the thickness is most evident.

For the cylindrical specimen, a different set-up was used (Figure 9b). A single camera (Nikon7100, 4000×6000 pixel resolution, equipped with a Nikkor 60 mm Micro lens, used at f/16) was mounted on a slewing ring in order to capture multiple pictures of the specimen at different angles. The specimen was a cylindrical sample of Grade X100 steel with an initial diameter of 8 mm. A detailed description of the procedure used to derive the 360-deg displacement together with the related error analysis is reported in [29]. In this case, to accurately reconstruct the surface displacement

(a)

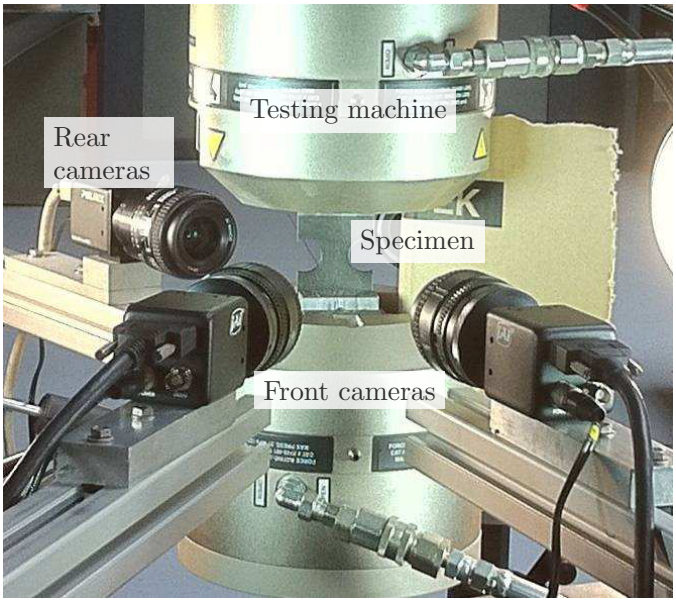

(b)

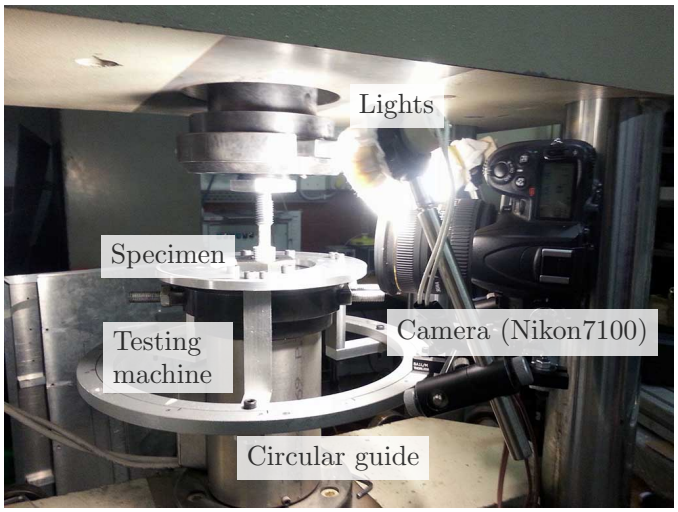

Figure 9: Experimental set-ups used for the flat and the cylindrical specimen.

field, the commercial software MatchID (http://matchidmbc.be/) was used to perform a large deformation DIC analysis.

As result of the stereo-DIC analysis, a set of measurement points with coordinates $\mathbf{X}_{DIC}$ and the corresponding 3D displacement field $\mathbf{u}_{DIC}$ were obtained for both tested geometries. These data were not directly used for the IMG method but they were first regularized using the *scatteredInterpolant* Matlab interpolation function.

The different steps of the volume reconstruction are listed below.

1. A regular grid of points with coordinates $\mathbf{X}_{S0}$ was defined over the specimen surface in the undeformed configuration. The displacement field $\mathbf{u}_{DIC}$ obtained from DIC was mapped over the regular grid using the interpolation function $\mathcal{I}$:

$$\mathbf{u}_{S0} = \mathcal{I}\left(\mathbf{u}_{DIC}, \mathbf{X}_{DIC}, \mathbf{X}_{S0}\right) \tag{9}$$

   where $\mathbf{u}_{S0}$ is the resulting displacement field. The coordinates $\mathbf{X}_{S1}$ of the grid points after deformation are obtained as:

$$\mathbf{X}_{S1} = \mathbf{X}_{S0} + \mathbf{u}_{S0} \tag{10}$$

2. The reconstruction algorithm described in Section 2 was used to obtain the internal points $\mathbf{X}_{V0}$ and $\mathbf{X}_{V1}$ starting from the corresponding surface points. The volume displacement field $\mathbf{u}_{V0}$ was then derived as:

$$\mathbf{u}_{V0} = \mathbf{X}_{V1} - \mathbf{X}_{V0} \tag{11}$$

3. As a final step, the volume displacement $\mathbf{u}_{V0}$ was projected over a 3D mesh of the specimen obtained using the mesh generator of

Abaqus. The displacement $\mathbf{u}_N$ of each node was obtained from the reconstructed displacement field using the interpolation function:

$$\mathbf{u}_N = \mathcal{I}\left(\mathbf{u}_{V0}, \mathbf{X}_{V0}, \mathbf{X}_N\right) \tag{12}$$

where $\mathbf{X}_N$ are the coordinates of the nodes. The FE software was then used as post-processing tool to display the 3D dispalcement and strain fields. It must be specified that no computation was performed because the displacement of each node was determined through the IMG procedure.

The procedure reported above was implemented for both experiments, the number of points corresponding to the different steps are listed in Table 2. For the flat specimen, for each face, the DIC measurement evaluated 4977 points that were then reshaped over a regular grid of 40×50, in the x and y directions, respectively. The IMG method reconstructed a total of 22000 points, corresponding to the nodes of the 3D mesh. For the cylindrical specimen, a very dense point cloud was obtained from the 360-deg measurement. Such points were used to reconstruct a regular grid of 28×29 points, in the θ and z directions, respectively. Then 8932 points were generated with the IMG method and they were used to retrieve the deformation of the 8410 nodes of the solid mesh. For the two studied cases, the deformation is large and the shape change due to necking is reasonably smooth, therefore the IMG method is not significantly affected by surface imperfections or noise. In case of highly localized behaviour or not smooth surfaces, a sensitivity analysis on the effect of noise is recommended.

The experimental results are discussed separately for the two tests in the next sections.

	Number of points			
	stereo-DIC	regular grid	IMG method	solid mesh
Flat spec.	4977	2000 (40×50)	22000	22000
Cylind. spec.	629104	812 (28×29)	8932	8410

Table 2: Number of points used in the various steps of the reconstruction process.

4.1. Flat specimen

Figure 10 illustrates the reconstruction of the volume deformation of the flat specimen. The initial undeformed configuration of the investigated portion of the specimen has a height of 16 mm, a width of 18 mm in the minimum section and a thickness of 8 mm. At the last step of deformation, a final height of 26.06 mm was reached and a localized necking occurred at the centre of the specimen.

In Figure 11, the maximum principal strain at the surface and within the specimen is plotted along the specimen width. The surface deformation is not symmetrical, a larger deformation is observed on the left side of the specimen, probably due to an initial uneven geometry of the specimen and/or to an asymmetrical application of the load during the test. When the reconstructed volume is sectioned along the longitudinal (Section A-A) and transverse (Section B-B) directions, it reveals the expected strain concentration that occurs in the central zone of the necking.

In order to better visualize the inner peak of strain, Figure 12 reports the plot of the maximum principal strain in the central section of the specimen as evaluated at the top, bottom and mid-plane surfaces, as a function of the section width. As expected, the strain distribution at the top and bottom surfaces, *i.e.* the values calculated from the back-to-back stereo-DIC, are similar. In contrast, the strain path reconstructed within the specimen has

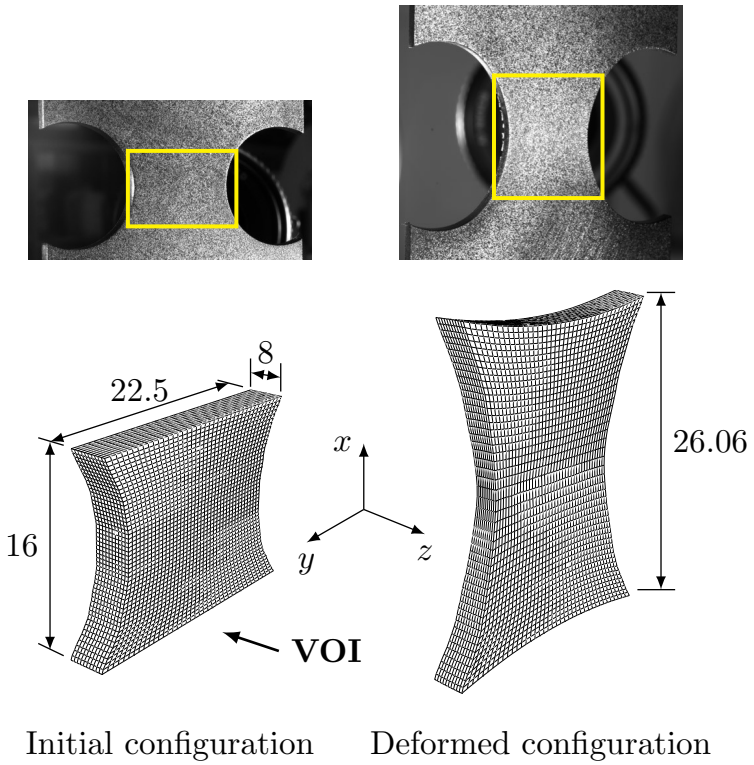

Figure 10: Reconstructed three-dimensional geometry for the flat specimen in the undeformed and deformed configuration and comparison with the experimental pictures of the specimens.

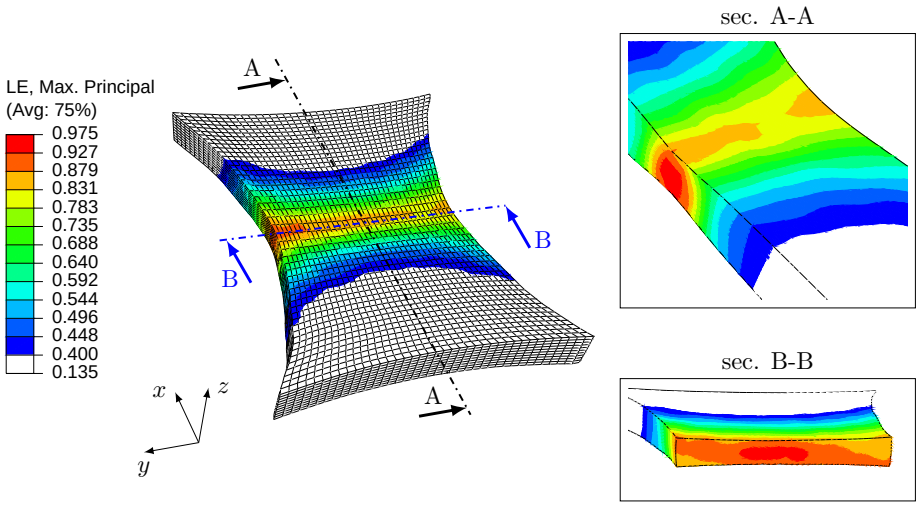

Figure 11: Longitudinal and transversal cross sections of the specimen showing the strain concentration.

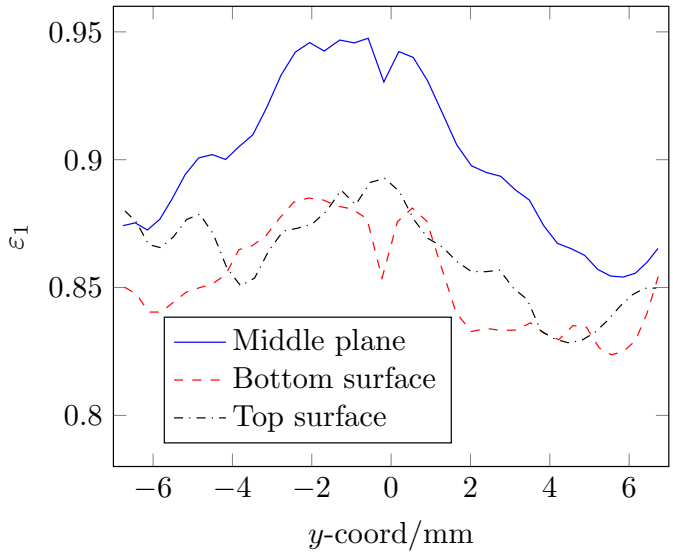

Figure 12: Comparison of the principal strain obtained on the middle plane and on the top and bottom surfaces along the specimen width (y-direction).

a value comparable to that of the surface measurement only at the edges of the specimen. In the central zone, an increase of about the 10% is observed, going from 0.85 to 0.95.

4.2. Cylindrical specimen

The reconstructed undeformed and deformed shapes of the cylindrical specimen are illustrated in Figure 13. In this case, the VOI is a central zone of 13.5 mm in length. At the considered deformed stage, a 17.47 mm longitudinal length was reached and a well developed localized necking was clearly visible in the central portion of the specimen.

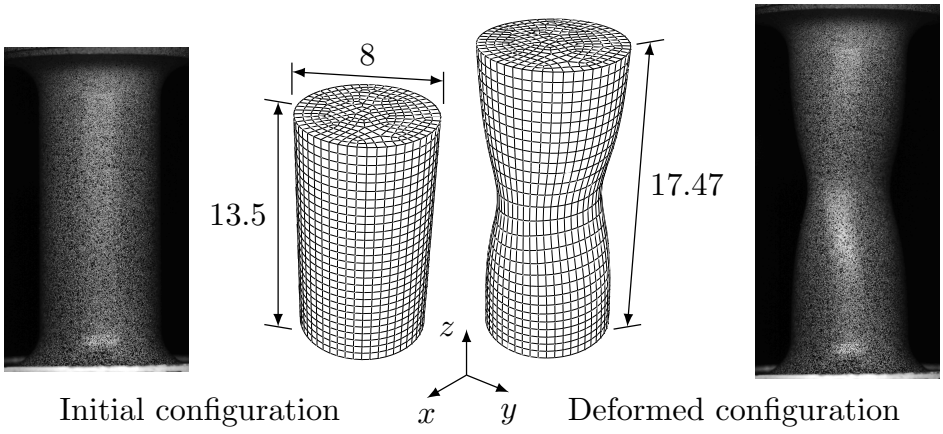

Figure 13: Three-dimensional reconstruction of the deformation of the cylindrical specimen and pictures of the specimen.

The used Grade X100 steel is homogeneous and rather anisotropic [7]. Because of the material anisotropy, the shape of the neck is not symmetrical. The strain localization inside the sample is shown in Figure 14 where the strain field over two of its cross sections is reported. As expected, the deformation contour pattern is not axi-symmetrical and the maximum strain is obtained in the centre of the specimen. The principal maximum strain

along different radial paths is plotted in Figure 15. In particular, three paths are shown, one along the major axis of the neck section, one along the minor axis and one at 45° with respect to the major axis. Depending on the considered angular position, the strain increase in the centre with respect to the surface ranges from +15% to almost +50%.

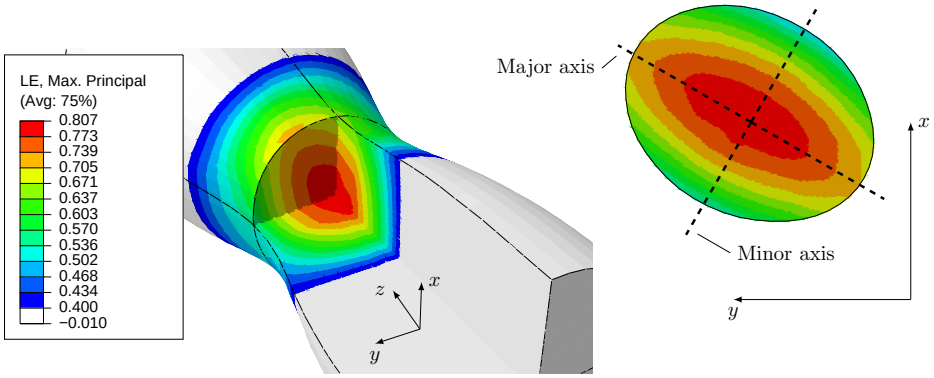

Figure 14: Strain distribution across two orthogonal cross sections of the specimen showing the strain concentration at its centre.

5. Discussion and Conclusion

This paper presented a Bézier curve-based reconstruction algorithm, named the IMG method, that allows to retrieve the three-dimensional displacement and strain field inside a solid, starting from surface displacement measurement data. The formulation presented here described in detail the procedure adopted for the reconstruction for flat or cylindrical specimens under tensile load. However a similar approach could be developed to study other deformation cases, *e.g.* torsion, bending, mixed-load, etc.

The IMG method, or a modified version of it, could be relevant in all cases where large deformation is encountered and the material is homoge-

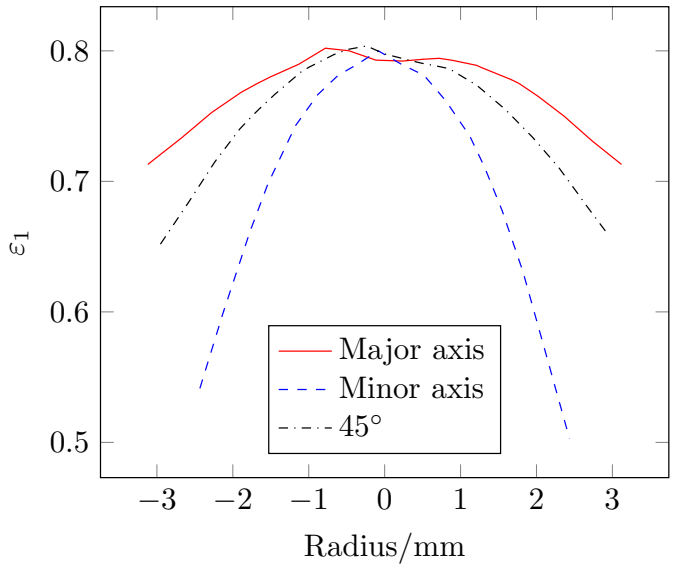

Figure 15: Plots of the principal strain along three different radial paths in the central section of the specimen.

neous. Since surface data are nowadays reasonably easy to obtain, it could be potentially applied in a large number of situations of engineering interest (*e.g.* biological tissues, soft materials, etc.). Nonetheless, the feasibility has to be conveniently verified on a case by case basis.

The strain localization within the necking region represents a suitable example that the proposed technique can be successfully applied to. On the other hand, in order to obtain acceptable results, the following remarks should be carefully taken into consideration:

- the raw displacement data obtained from stereo-DIC are usually not suitable to be directly used with the reconstruction algorithm. As shown in Section 4, a smoothing and a remap of the displacement over a regular grid could be necessary. Since interpolation is involved, the starting measurement points should be denser than the final regular

grid in order to reduce the interpolation error.

- The size of the regular mesh used to define the starting surface points in the reconstruction algorithm should be properly chosen. As a practical solution, the mesh generator of commercial FE codes can be conveniently used to this purpose.

- In the discussed examples, the basic built-in Matlab function *normsurf* was used to find surface normals and the function *scatteredInterpolant* was used to interpolate points. The use of more sophisticated routines and smoothing algorithms could be implemented to investigate their possible beneficial effect on the robustness of the IMG method, especially in the presence of large measurement noise.

- A rigorous error analysis of the reconstruction algorithm was beyond the scope of this paper. In order to assess the feasibility of application to material identification, a detailed study should be performed to evaluate the impact of the reconstruction errors on the material identification, using for instance simulated experiments as in [40, 41].

In summary, the paper describes a reconstruction algorithm able to derive the displacement and strain fields in the bulk of a solid sample. The proposed method was validated using numerical models and then applied to real experiments to retrieve the strain concentration inside the necking region of metal specimens subjected to large deformations The following concluding considerations can be made:

- the proposed method can be applied to flat or cylindrical specimens subjected to large deformation;

- the numerical validation proved that the reconstruction algorithm is feasible even if the material is highly anisotropic and the necking shape produces a complex three-dimensional stress-strain state;

- the method was applied to real experiments. The strain concentration inside the neck is considerable, especially for the cylindrical specimen, where an increase up to 50% was observed in the inner part with respect to the surface;

- the experimental technique used to obtain the displacement field over the solid surface plays an important role for the accuracy of the reconstruction. In particular, the spatial resolution of the surface measurement is very important.

- The authors note that the proposed method, which does not use boundary condition information as part of the process, is strictly applicable in situations where the problem is of the type known as "geometrically determined". These problem types include important applications such as beams, plates, and shells that do not have flaws, internal cut-outs or geometric complexities. In these cases, it is well-known that the interior (through-thickness) deformation can be estimated from surface deformation data (including curvature). The extension of the method for use in a hybrid approach with analytic or computational algorithms to address the effect of additional complexities will require additional research in the future.

In future, the method will be coupled with inverse identification techniques to identify the constitutive parameters of plasticity and damage models.

References

[1] M. Grédiac and F. Hild. *Full-field measurements and identification in solid mechanics*. John Wiley & Sons, 2012.

[2] M.A. Sutton, J.-J Orteu, and H.W. Schreier. *Image correlation for shape, motion and deformation measurements*. Springer New-York, 2009.

[3] D. Amodio, G. B. Broggiato, F. Campana, and G. M. Newaz. Digital speckle correlation for strain measurement by image analysis. *Exp Mech*, 43(4):396–402, 2003.

[4] O. Faugeras. *Three-dimensional computer vision: a geometric viewpoint*. MIT press, 1993.

[5] V. Tvergaard. Necking in tensile bars with rectangular cross-section. *Comput Method Appl M*, 103(1-2):273–290, 1993.

[6] F.A. Nichols. Plastic instabilities and uniaxial tensile ductilities. *Acta Metall Mater*, 28(6):663–673, 1980.

[7] L. Cortese, T. Coppola, F. Campanelli, F. Campana, and M. Sasso. Prediction of ductile failure in materials for onshore and offshore pipeline applications. *Int J Damage Mech*, 23(1):104–123, 2014.

[8] Y. Bai and T. Wierzbicki. A new model of metal plasticity and fracture with pressure and lode dependence. *Int J Plasticity*, 24(6):1071–1096, 2008.

[9] S. Cooreman, D. Lecompte, H. Sol, J. Vantomme, and D. Debruyne.

Identification of mechanical material behavior through inverse modeling and dic. *Exp Mech*, 48(4):421–433, 2008.

[10] J. Kajberg and G. Lindkvist. Characterisation of materials subjected to large strains by inverse modelling based on in-plane displacement fields. *Int J Solids Struct*, 41:3439–3459, 2004.

[11] A. Needleman. Material rate dependence and mesh sensitivity in localization problems. *Comput Method Appl M*, 67(1):69–85, 1988.

[12] M. Grédiac and F. Pierron. Applying the virtual fields method to the identification of elasto-plastic constitutive parameters. *Int J Plasticity*, 22:602–627, 2006.

[13] J.-H. Kim, A. Serpantié, F. Barlat, F. Pierron, and M.-G. Lee. Characterization of the post-necking strain hardening behavior using the virtual fields method. *Int J Solids Struct*, 50(24):3829–3842, 2013.

[14] F. Pierron and M. Grédiac. *The Virtual Fields Method*. Springer New York, 2012.

[15] M. Rossi and F. Pierron. Identification of plastic constitutive parameters at large deformations from three dimensional displacement fields. *Comput Mech*, 49:53–71, 2012.

[16] B. K. Bay, T. S. Smith, D. P. Fyhrie, and M. Saad. Digital volume correlation: three-dimensional strain mapping using X-ray tomography. *Exp Mech*, 39(3):217–226, 1999.

[17] T. S. Smith, B. K. Bay, and M. M. Rashid. Digital volume correlation including rotational degrees of freedom during minimization. *Exp Mech*, 42(3):272–278, 2002.

[18] M. Gates, J. Lambros, and M.T. Heath. Towards high performance digital volume correlation. *Exp Mech*, 51(4):491–507, 2011.

[19] C. Franck, S. Hong, S.A. Maskarinec, D.A. Tirrell, and G. Ravichandran. Three-dimensional full-field measurements of large deformations in soft materials using confocal microscopy and digital volume correlation. *Exp Mech*, 47(3):427–438, 2007.

[20] A. Germaneau, P. Doumalin, and J.-C. Dupré. 3D strain field measurement by correlation of volume images using scattered light: recording of images and choice of marks. *Strain*, 43(3):207–218, 2007.

[21] S. Roux, F. Hild, P. Viot, and D. Bernard. Three-dimensional image correlation from x-ray computed tomography of solid foam. *Compos Part A-Appl S*, 39(8):1253–1265, 2008.

[22] S. M. Atay, C. D. Kroenke, A. Sabet, and P. V. Bayly. Measurement of the dynamic shear modulus of mouse brain tissue in vivo by magnetic resonance elastography. *J Biomech Eng*, 130(2):021013, 2008.

[23] M. Rossi and F. Pierron. Identification of the plastic behaviour in the post-necking regime using a three dimensional reconstruction technique. *Key Eng Mater*, volume 504, pages 703–708. Trans Tech Publ, 2012.

[24] J.-E. Dufour, F. Hild, and S. Roux. Shape, displacement and mechanical properties from isogeometric multiview stereocorrelation. *J Strain Anal Eng*, volume 50(7): 470–487, 2015.

[25] Y. Wang, P. Lava, S. Coppieters, P.V. Houtte, and D. Debruyne. Application of a multi-camera stereo DIC set-up to assess strain fields in

an Erichsen test: Methodology and validation. *Strain*, 49(2):190–198, 2013.

[26] J.-J. Orteu, F. Bugarin, J. Harvent, L. Robert, and V. Velay. Multiple-camera instrumentation of a single point incremental forming process pilot for shape and 3D displacement measurements: methodology and results. *Exp Mech*, 51(4):625–639, 2011.

[27] F. Heuer, H. Schmidt, and H.-J. Wilke. The relation between intervertebral disc bulging and annular fiber associated strains for simple and complex loading. *J Biomech*, 41(5):1086–1094, 2008.

[28] D. Spera, K. Genovese, and A. Voloshin. Application of stereo-digital image correlation to full-field 3-D deformation measurement of intervertebral disc. *Strain*, 47(s1), 2011.

[29] K. Genovese, L. Cortese, M. Rossi, and D. Amodio. A 360-deg digital image correlation system for materials testing. *Opt Laser Eng*, 82:127–134, 2016.

[30] A. K. Asundi, C.-S. Chan, and S. R. Marokkey. 360-deg profilometry: new techniques for display and acquisition. *Opt Eng*, 33(8):2760–2769, 1994.

[31] H. Guo and M. Chen. Multiview connection technique for 360-deg three-dimensional measurement. *Opt Eng*, 42(4):900–905, 2003.

[32] P. Badel, K. Genovese, and S. Avril. 3D residual stress field in arteries: Novel inverse method based on optical full-field measurements. *Strain*, 48(6):528–538, 2012.

[33] M. Sasso, M. Rossi, G. Chiappini, and G. Palmieri. Sheet metals testing with combined fringe projection and digital image correlation. In *Proceedings of the 2009 SEM annual conference*, volume 182, 2009.

[34] J. M. Nguyen, T. N.and Huntley, R. L. Burguete, and C. R. Coggrave. Multiple-view shape and deformation measurement by combining fringe projection and digital image correlation. *Strain*, 48(3):256–266, 2012.

[35] P. W. Bridgman. *Studies in large plastic flow and fracture*, volume 177. McGraw-Hill New York, 1952.

[36] G. Mirone. A new model for the elastoplastic characterization and the stress-strain determination on the necking section of a tensile specimen. *Int J Solids Struct*, 41(13):3545–3564, 2004.

[37] C. Beder and W. Förstner. Direct solutions for computing cylinders from minimal sets of 3D points. *Computer Vision–ECCV 2006*, pages 135–146, 2006.

[38] R. Hill. A theory of the yielding and plastic flow of anisotropic metals. *P Roy Soc A-Math Phy*, 193:281–297, 1948.

[39] L. Cortese, F. Nalli, and M. Rossi. A nonlinear model for ductile damage accumulation under multiaxial non-proportional loading conditions. *Int J Plasticity*, 85:77–92, 2016.

[40] M. Badaloni, M. Rossi, G. Chiappini, P. Lava, and D. Debruyne. Impact of experimental uncertainties on the identification of mechanical material properties using DIC. *Exp Mech*, 55(8):1411–1426, 2015.

[41] M. Rossi, P. Lava, F. Pierron, D. Debruyne, and M. Sasso. Effect of

DIC spatial resolution, noise and interpolation error on identification results with the VFM. *Strain*, 51(3):206–222, 2015.